Lab on a Chip

PAPER

View Article Online
View Journal | View Issue

Cite this: *Lab Chip*, 2026, **26**, 403

Navigation and selection of spermatozoa in a radial flow microfluidic device

Ali Karimi, Xieergai Jiang and Alireza Abbaspourrad *

Received 7th August 2025,
Accepted 24th November 2025

DOI: 10.1039/d5lc00778j

rsc.li/loc

The rheotactic behavior of spermatozoa in an outward radial flow was studied using a combination of theoretical and experimental approaches. Simulations suggested that at moderate flow rates, spermatozoa exhibited directed migration towards the flow origin, while at higher flow rates, the spermatozoa were predicted to display rotational rheotaxis, circling the origin while gradually moving inward, delaying their arrival at the center. Leveraging these findings, we developed a microfluidic device combining radial flow with strategically placed contracted pathways for efficient sperm selection, the sperm unidirectional navigation chip (SUN chip). This platform processed raw bovine semen to isolate highly motile (up to 98% motility) and vital spermatozoa suitable for assisted reproductive technologies. The yield of motile sperm retrieval for the SUN chip is ~30%, and the cells in the processed population were 50% faster on average compared to raw semen. Our results demonstrate the potential of radial flow microfluidics to enhance sperm selection processes and can be used to investigate other microswimmer dynamics.

Introduction

Spermatozoa transverse through and interact with the female reproductive tract (FRT), where they are exposed to a complex microenvironment on their way to the oocyte complex.[1–3] The biochemical environments that sperm encounter as they transverse the epithelium in the FRT influence their vitality,[4] capacitation level,[4] and ultimately their ability to fertilize the oocyte.[5] In addition to the variations in biochemical signals, the physical maze-like environment of the epithelium, particularly the fallopian tube, alter sperm–surface hydrodynamic interactions.[6–15] The secretion of ovulatory fluids influences this interaction by introducing dynamic conditions associated with fluid flow such as rheotaxis[16–18] and viscosity.[19,20]

Previous studies have focused on two-dimensional *in vitro* models of the FRT epithelium such as straight micro-pathways,[12,16] strictures,[7,21] and curvatures[6] to emulate spermatozoa navigation. Wall swimming and rheotaxis, swimming against the flow to the upstream, can be induced using a straight microchannel with a uniform shear rate along the fluid stream lines and the presence of side walls.[12,16] Shear rate gradients and slanted walls induce a butterfly-like motion in sperm under channel contraction.[7] The FRT is a complex microenvironment that sperm need to navigate while being exposed to variable flow fields,[1,22] which are generated by the narrow gaps and folds of the epithelia that range from 10 to 100 μm (ref. 1 and 23) and the curved structures that progressively narrow toward the site of fertilization.[6] Different geometrical features, such as strictures[7,21] and curvatures,[6] produce distinct flow fields even at the same flow rate. Although no *in vivo* evidence is available for human and bovine, experimental measurements of flow rates post mating within mice reproduction tracts indicate a fluid flow with an average velocity of ~18 μm s^{-1}.[24] Given that the fallopian tube exhibits a complex architecture of such features, we anticipate highly variable and spatially heterogeneous flow patterns along its length. The rheological properties of mucus are also variable along the fallopian tube and throughout the menstrual cycle with the dynamic viscosity ranging from 1 mPa s to 10^3 mPa s.[25] *In vitro* observations showed that viscoelasticity of the surrounding fluid suppresses the three-dimensional beating of sperm.[26,27] To assist with understanding these complex flow conditions, computational modeling has been used to predict the migration of microswimmers, including sperm, under complex flow conditions.

Computational modeling is a powerful technique to study the swimming behavior of microswimmers including *Escherichia coli*[28–30] and spermatozoa.[7,31–33] These techniques have been used to predict and explain spermatozoa locomotion in the absence[13,34] and presence[7,35–37] of external fluid flow. Computational modeling allows for prediction of and confirmation of observed swimming patterns within different microenvironments. To reconstruct the environments predicted by computational modeling, microfluidics technology has been used to construct *in vitro*

Department of Food Science and Technology, Cornell University, Ithaca, NY 14853, USA. E-mail: alireza@cornell.edu

models mimicking the features of the FRT.[3,38,39] Together, computational modeling and microfluidics enable a wide range of experiments designed to simulate the natural selection processes that sperm undergo in the female reproductive tract, thereby improving sperm selection for infertility treatments.[40]

Microfluidic devices have been used for selecting sperm based on rheotactic behavior[8,35,41–45] and boundary following behavior.[15,46–49] Spermatozoa isolated by microfluidic techniques exhibited higher motility and less DNA fragmentation compared to sperm isolated using the centrifugation method or swim-up methods.[50–54] Selection of high quality spermatozoa increases the chances for successful fertilization in assisted reproductive technologies, resulting in healthier embryo development and more positive pregnancy outcomes.[51,55–58] Major drawbacks of the current rheotaxis-based microfluidic devices are low throughput, small processing volume, and low concentration yields, as well as some device fabrication challenges.

We hypothesized that using a radial flow-based microfluidic device with no side walls would reduce areas where dead spermatozoa accumulate and increase separation throughput by providing a radial shear rate gradient to separate motile spermatozoa from dead or non-motile spermatozoa. A radial flow system would also enable a highly distributed flow and therefore larger processing volumes.

To create a radial flow-based device, we predicted the bovine spermatozoa navigational pattern in a radial flow while changing the shear strength of the flow. At a moderate flow rate, spermatozoa navigate unidirectionally toward the flow origin, while higher flow rates cause the spermatozoa to rotate around the origin while progressively approaching it; we call this rotational rheotaxis. By combining radial flow rheotaxis with localized strictures,[7,8] we designed a sperm unidirectional navigation chip, the SUN chip, (Fig. 1) with high throughput (0.75 mL h^{-1}), motility (98%), and a final spermatozoa concentration of 8 million per milliliter. The cells in the isolated population were 50% faster on average compared to the raw semen sample.

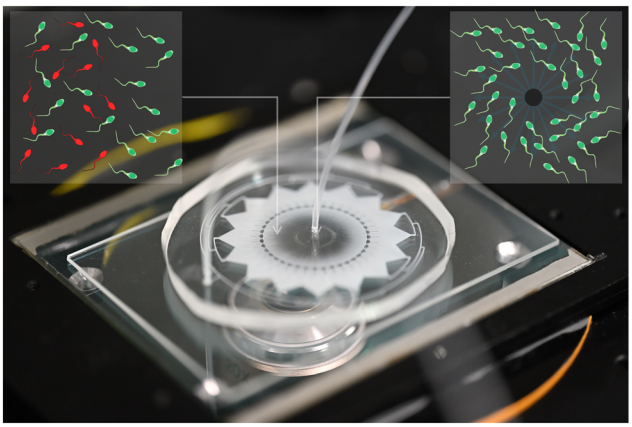

Fig. 1 Sperm unidirectional navigation chip. Motile sperm actively navigate within a radial flow field originating from the center, leading to their accumulation near the center, while immotile sperm are passively carried away by the flow.

Results and discussion

Sperm navigation in a radial flow field

As sperm navigate the folded epithelium of the fallopian tube, they encounter highly variable fluid flow fields.[1,7,21] Although *in vivo* evidence for radial flow in the female reproductive tract is lacking, the complex geometry of adjacent epithelial folds likely generates localized radial flow between neighboring surfaces. The radial flow can be assumed as the flow between two parallel, circular disks featuring a symmetrical, radially directed flow pattern, with the velocity increasing from the center toward the edges (Fig. 2a). The fluid velocity v_f and wall shear rate γ for an outward laminar radial flow in the space between two parallel circular disks are inversely correlated with the radius: $v_f, \gamma \propto r^{-1}$ (ref. 59) (Fig. 2b). This enables us to generate a shear rate gradient without using side walls; the radial shear generates its own shear rate gradient.[7,44]

The two-dimensional navigation of sperm in an external flow can be modeled by superposition of the fluid velocity and the sperm self-propulsion velocity (Fig. 2c). The time-dependent location vector of a sperm $\vec{z}_i = (x_i, y_i)$ with intrinsic propulsive velocity of v_s in a two-dimensional fluid flow field $\vec{v}_f$ is modeled by

$$\frac{d\vec{z}_i}{dt} = \vec{v}_f + v_s \begin{pmatrix} -\sin(\beta_i + \varphi_i) \\ \cos(\beta_i + \varphi_i) \end{pmatrix} \quad (1)$$

where β_i is the angle between the positive x-axis and the sperm location vector (x_i, y_i), and φ_i is the angle between sperm direction $\vec{s}_i$ and radial axis (eqn (2) and (3)). Here, i denotes the index of the individual sperm.

$$\beta_i = \arctan\left(\frac{y_i}{x_i}\right) \quad (2)$$

$$\varphi_i = \frac{-\vec{z}_i \cdot \vec{s}_i}{|\vec{z}_i|} \quad (3)$$

The rheotactic reorientation of a pusher microswimmer attributed to the external linear Stokes flow in the proximity of a wall is modeled by an overdamped equation[17,60]

$$\frac{d\varphi_i}{dt} = -\omega - A\gamma(x,y)\sin(\varphi_i) \quad (4)$$

where ω is the angular frequency associated with clockwise trajectory of sperm, A is a constant related to microswimmer geometry, and γ is the local fluid shear rate. Eqn (4) is known as the Adler equation,[61] in which the solution is a saddle-node bifurcation. Four scenarios can be defined based on the shear rate magnitude compared to the critical shear rate γ_c: 1) $\gamma < \gamma_c$: the navigation is dominated by intrinsic circular motion, 2) $\gamma = \gamma_c$: unstable navigation, 3) $\gamma > \gamma_c$: stable

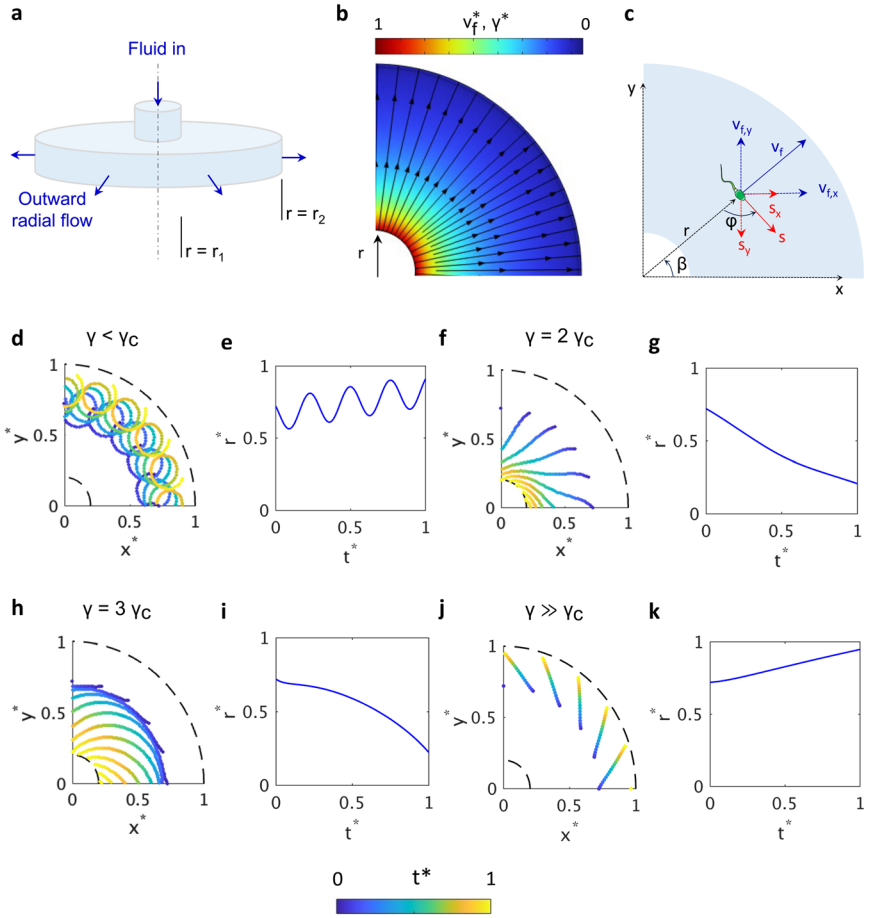

Fig. 2 Modeling sperm navigation in an outward radial flow field between two parallel, circular disks. (a) The flow is generated by a pressure difference between inner and outer radii r_1 and r_2, respectively. (b) The calculated normalized fluid velocity v^*_f and shear rate γ^* decay with r. Streamlines and arrows show the fluid velocity direction. (c) Schematic of sperm locomotion in the radial flow with depicted variables. r is the radial distance of sperm from the center, s shows the sperm orientation vector, and v_f is the fluid velocity vector. Sperm trajectories and time evolution analysis of average sperm radial location under radial flow strength corresponding to local shear rates of $\gamma = 0.5\gamma_c$ (d and e), $\gamma = 2\gamma_c$ (f and g), $\gamma = 3\gamma_c$ (h and i), and $\gamma = 8\gamma_c$ (j and k) measured at $r^* = r/r_2 = 0.75$. $\gamma_c = 3.03\ s^{-1}$ is the critical shear rate for rheotactic navigation. All sperm are considered identical pusher microswimmers with propulsive velocity of 100 μm s^{-1} released at $r^* = 0.75$. Time and dimensions are normalized with respect to their maximum values for enhanced visualization. Sperm location at each time step is color-coded indicating the time progression.

upstream navigation, and 4) $\gamma \gg \gamma_c$: sweeping away by strong fluid flow.

The radial domain inner radius r_1 and outer radius r_2 are 900 μm and 2500 μm, respectively. The cell distance from the flow origin ($r_i = ||z_i - z_0||$, z_0 is the location of flow origin) and time are normalized with respect to r_2 and total simulation time t_f ($r^* = r_i/r_2$ and $t^* = t/t_f$). The normalized radius is the distance from center divided by r_2. Trajectory predictions were performed on twenty identical sperm with constant $v_s = 100$ μm s^{-1} and initial orientation radially distributed within the domain at a constant radius of $r^* = 0.75$.

For bovine sperm, ω, A, and γ_c are estimated as 0.36 s^{-1}, 0.118, 3.03 s^{-1}, respectively.[17] Local values of γ and v_f values are imported from computational simulation of corresponding fluid domain and calculated for a cut plane situated 10 μm above the domain floor considering a channel height (h) of 200 μm (Fig. 2b), $r_1 = 900$ μm, and $r_2 = 2500$ μm in COMSOL software. We defined the strength of radial flow as the ratio of local shear rate calculated from simulation and the critical shear rate ($\gamma_c = 3.03\ s^{-1}$).[17] Flow strength values of $0.5\gamma_c$, $2\gamma_c$, $4\gamma_c$, and $8\gamma_c$, corresponding to local fluid velocities of 25, 100, 200, and 400 μm s^{-1} were used for flow-dependent navigation of sperm (Movies S1–S4). Note that the velocity and shear rate values are calculated at $r^* = 0.75$. In shear rates less than γ_c (Fig. 2d), the circling bias dominates sperm motion,[17] and the weak flow only pushes the sperm outward. The sperm continues its circling motion while being swept away (Fig. 2e). In shear rates exceeding γ_c, sperm change their orientation toward the center point and start to follow a curved trajectory until reaching the inner boundary (Fig. 2f). The curvature of radial position (Fig. 2g) indicates that the sperm's inward movement slows as it approaches the flow origin due to increased fluid velocity but remains in

a suitable range for rheotaxis. Increasing the flow strength to $\gamma = 3\gamma_c$ results in a new navigation where sperm are navigating toward the center, however, the high fluid velocity induces a rotation around the center of the device where the flow originates (Fig. 2h). The orientation of sperm until $t^* \approx 0.25$ is approximately perpendicular to the r^* axis and the net swimming velocity increases as the sperm approaches the center of the device (Fig. 2i). This rotational rheotaxis, where the sperm orientation is approximately perpendicular to the radial axis, is particularly noticeable at greater distances from the device center. The non-linear trajectories observed suggest rheotactic motion, indicating that the final swimming orientation of the sperm is dependent on the local shear rate and fluid velocity. This behavior leads to an autonomous hydrodynamic retention of sperm near the flow origin. As the flow strength increases, sperm are progressively displaced from their initial positions and eventually swept out of the outer boundary (Fig. 2j). In this regime, the trajectories become linear, reflecting the absence of rheotactic motion (Fig. 2k). Only healthy sperm exhibit unidirectional movement toward the center, while dead, damaged, or slower sperm and other particles and debris are flushed away (Note S1). The shape of the sperm trajectory indicates the cooperative effect of sperm propulsive velocity and the local fluid shear rate and velocity (Fig. S1).

Rotational rheotaxis was experimentally investigated using a microfluidic device. Due to the long-range motion of sperm while undergoing rotational rheotaxis, it was impossible to capture the full trajectory of rotation within the microscopic observation window. Therefore, we tracked several representative bovine sperm cells swimming within a radial flow in a microfluidic device with similar dimensions to the geometry of the model (r_1 = 900 μm, r_2 = 2500 μm, h = 200 μm). Slight modifications were made to handle the inlet tubing and control the sperm migration (Fig. 3a). The temperature was controlled using a heated stage maintained at 37 °C. The inlet fluid flow rate was kept constant at 1 mL h^{-1} because we started to observe the rotational rheotaxis at this flow rate. The observation window is ~1.5 mm away from the flow origin (Fig. 3b). To experimentally determine the flow origin, we tracked the passive debris particles that are naturally present in raw semen (Fig. 3c). We estimated the flow origin by fitting lines to the trajectories of each particle and identifying their intersection points. Radial streamlines were then interpolated between the experimental particle trajectories (dashed lines in Fig. 3c). The sperm trajectories are color-coded according to normalized time t^* (Fig. 3c).

Due to variability in motility within the sperm population, we observed two primary migratory behaviors, consistent with predictions from our computational model. First, some sperm progressively swim against the fluid flow, moving toward the flow origin (Fig. 3d). For example, the trajectory of cell #1 mirrors the pattern shown in Fig. 2f; its radial distance decreases over time, indicating unidirectional movement toward the flow origin (Fig. 3e). In contrast, cell #2 exhibits rotational behavior, maintaining a roughly constant radial distance (Fig. 3e). The motility pattern of cell

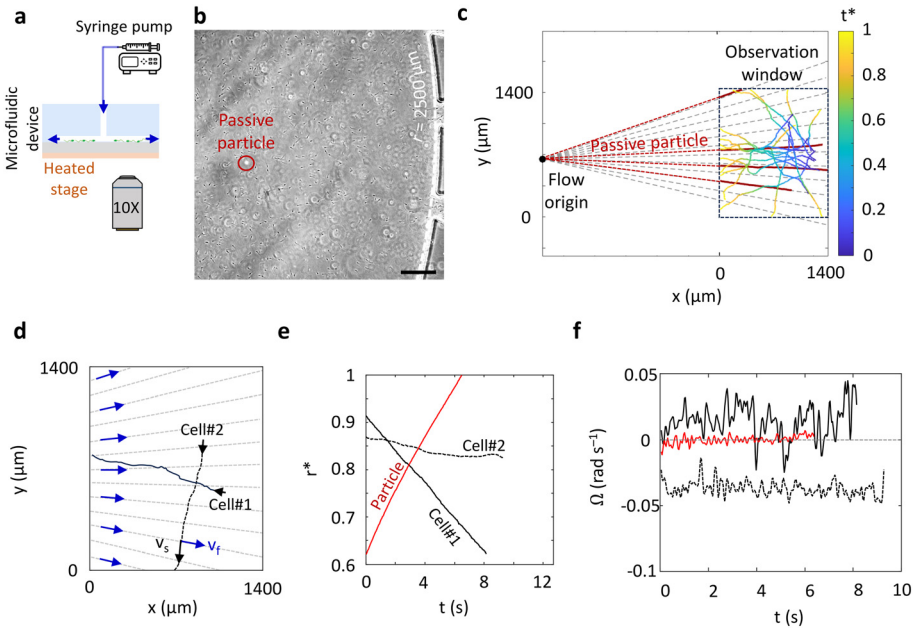

Fig. 3 Experimental evidence for rotational rheotaxis in a radial flow field. (a) Schematic showing the cross-section of the microfluidic device mounted on an inverted microscope. The flow is generated by a syringe pump. Scale bar: 200 μm. (b) Representative image of sperm in the radial flow. Passive particles are used for obtaining the local flow streamline. (c) Estimating the origin of flow location using passive trackers. Representative sperm trajectories are color-coded with respect to time progression (t^*). (d) Two types of trajectories observed in the radial flow with sperm propulsion of v_s and local fluid velocity of v_f. (e) Radial location of sperm and a passive particle over time. (f) Instantaneous angular velocity $\Omega(t)$ is non-zero and larger for sperm undergoing full rotational rheotaxis moving perpendicular to the flow direction.

#2 is reminiscent of the scenario in Fig. 2h; the sperm propulsion direction (v_s) is nearly perpendicular to the flow direction (v_f) (Fig. 3d). The cell undergoing rotational rheotaxis has a non-zero angular velocity confirming the radial motion (Fig. 3f). Overall, these results provide direct experimental evidence of rotational rheotaxis and highlight the distinct migrational patterns of sperm in the radial flow.

Design of the sperm unidirectional navigation chip

Rheotaxis has been used as a selection pressure to isolate sperm with high motility and low DNA fragmentation.[62] To exploit the ability of radial flow to separate motile from immotile sperm, we designed the sperm unidirectional navigation (SUN) chip, guided by our computational results. In a radial flow field, the shear rate decreases with the distance away from the flow origin; thus, sperm may be carried away by the fluid, as observed in the swimming mode in Fig. 2d, if the local shear rate falls below a critical threshold. In the SUN chip, we combined a radial flow design with two concentric rings of shear rate barriers,[21] which locally enhanced the shear rate to induce sperm rheotaxis (Fig. 4b and d). The SUN chip design consists of four main regions: 1) flow origin barriers, 2) first ring of shear rate barriers, 3) second ring of shear rate barriers, and 4) outlet funnels. The device was fabricated from polydimethylsiloxane (PDMS) using conventional soft lithography techniques.[63]

The barriers in regions 2 and 3 have a gap size of 100 μm and an apex angle of 45°. Within a flow range of 600–1200 μL h^{-1} these barriers produced localized shear rates that met the required minimum for rheotaxis.[17] The gap size of 100 μm was chosen because it is within the range of reported spacing between epithelial surfaces in the female reproductive tract.[1,23] The shear rate barriers act both as healthy sperm retainers, by capturing the sperm that is being washed away, and imposing selection on the sperm population based on the ability of the sperm to pass the areas of high shear rate[7] (Fig. 4c). The geometry of the barriers is optimized to direct the sperm toward the flow origin[21] where they are retained until the end of the separation experiment (Fig. 4d). Therefore, sperm unidirectionally navigate toward the flow origin in the SUN chip and are maintained within the chip through rotational rheotaxis.

The migration of bovine sperm while moving in the SUN chip was observed and filmed on a phase-contrast microscope. Sperm trajectories were tracked by analyzing ten consecutive images acquired at 30 frames per second, allowing us to observe their movement near different regions of the chip at a flow rate of 1 mL h^{-1}. This flow rate corresponds to an average local shear rate of 6.5 s^{-1} inside barrier gaps, which exceeds the threshold shear rate for rheotaxis of 3.03 s^{-1}, ensuring the emergence of sperm rheotactic behavior[17] within the pathways of region 2 and 3. At region 1, flow is distributed through six identical channels with a width of 100 μm. Based on modulated sperm–surface–fluid interaction, these barriers prevent sperm from entering

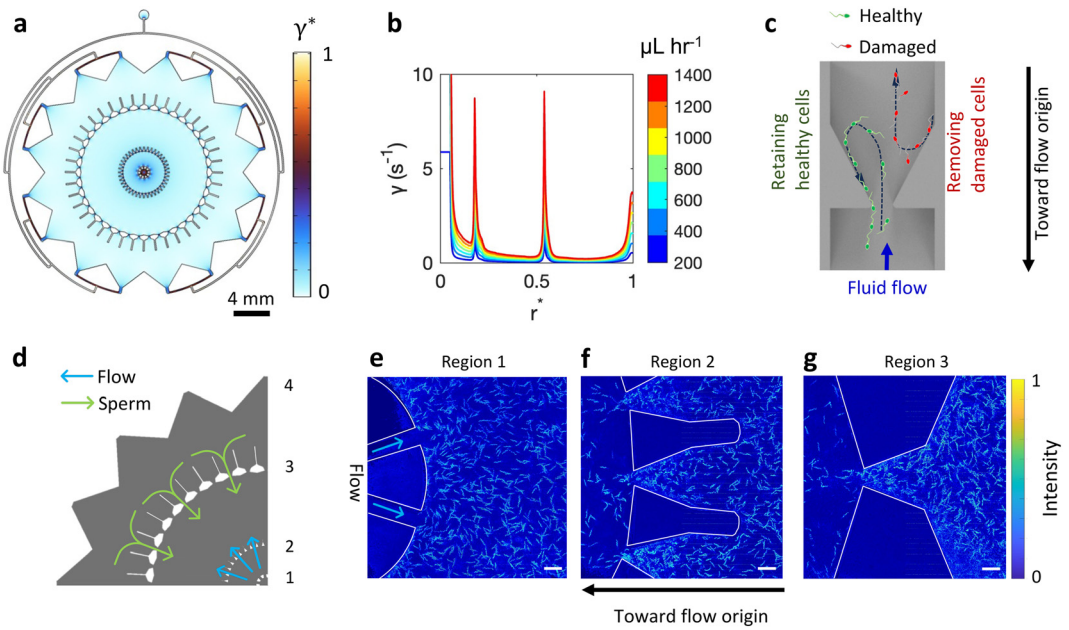

Fig. 4 Design of the sperm unidirectional navigation (SUN) chip. (a) Shear rate profile in the SUN chip showing variable shear rate regions. Medium flow enters from central port. The color bar indicates the shear rate normalized by maximum value. (b) Shear rate profile along the radial axis under different flow rates. The radius axis in the shear rate profile is normalized with respect to the total radius of the main chamber from the center to the outlet funnels. Color bars indicate the flow rate magnitude. Peaks show the location of barriers. (c) The single stricture generates a local shear rate resulting in directing motile sperm toward upstream and while blocking the passage of damaged cells. (d) Schematic view of a quarter of the design showing the direction of fluid flow and sperm migration within different regions 1–4. Upstream sperm navigation in regions 1 (e), 2 (f), and 3 (g) under an inlet flow rate of 1 mL h^{-1}. Images are constructed by processing ten consecutive frames of sperm motion at 30 frames per second and colorizing with respect to the pixel intensity for better visualization. The color bar indicates the pixel intensity.

the inlet medium tube through the high shear rate[22] (Fig. 4e and Movie S6). Shear rate barriers in regions 2 and 3 have identical gap sizes and apex angles (Fig. 4f and g). The higher density of cells behind the rings indicates the selection applied on the population to prevent damaged cells from passing the barriers and remaining in the chip. The barrier in regions 2 and 3 also functions as a pump directing cells toward the flow origin (Movies S7 and S8 and Fig. 4f and g).

We experimentally investigated the critical flow rate required for rheotaxis in the barriers. The local shear rate inside barrier gaps must exceed 3.03 s^{-1} to induce rheotactic navigation,[17] which happens for the total inlet flow rates more than approximately 600 μL h^{-1} (Fig. 4b). To confirm this, we monitored the sperm navigation through a barrier in region 2 under different flow rates from 200 to 1800 μL h^{-1} (Fig. 5a–e).

Rheotactic navigation begins at a flow rate of 600 μL h^{-1} (shear rate of 4 s^{-1} inside strictures), increasing the flow rate further elevates barrier selectivity; a higher shear rate impedes the ability of low motility sperm to pass and changes the sperm's navigational pattern. Higher shear rates generate a butterfly motion that prevents sperm, even the most motile, from navigating upstream as observed previously.[7] The barriers in region 3 are similar to those in region 2, but with specific modifications. The comet-like structures in the barriers of both regions increase the surface boundaries, thereby enhancing the probability of capturing sperm from the bulk fluid.[15,32] In region 3, the comet structures are further enlarged to maximize sperm capture and facilitate their reorientation toward the flow origin, preventing them from being swept away by the flow. The fluid exits the chip after going through a branched flow distributor connected to funnels (Fig. 3b region 4). Details of the SUN chip design and dimension specifications are provided in Fig. S2 of the SI.

Sperm selection performance of the SUN chip

We used the SUN chip to isolate motile sperm from the raw bovine semen sample. The processing volume of the main selection chamber (excluding the distributor channels) is 150 μL and the total loaded volume including the distributor channels and the tubing is 180 μL. The operation of the SUN chip consists of three steps: 1) filling the chip with the raw semen sample, 2) washing the semen with medium flow from the central port using a syringe pump, and 3) extracting the selected sperm population using a pipet (Fig. S3 in the SI). This procedure allows us to remove dead or immotile sperm, as well as other particles, including cryopreservatives, from the semen sample. During the experiment, the microfluidic device was maintained at 37 °C on a hotplate. To simulate the washing step and obtain the required washing time, we filled the chip with a dye and washed the chip with water at 1 mL h^{-1}. We selected a total dispensed medium volume of 300 μL for the complete washing step, as semen contains particles and other debris that may adhere to the surface and otherwise prolong the washing process (Fig. S3b and c and Movie S5).

To evaluate the selection efficiency of the SUN chip, we collected sperm samples separated at different flow rates (0.8, 1.0, 1.2, 1.5 mL h^{-1}) and subsequently analyzed their properties. We isolated sperm with 93 ± 6% motility at flow rates of 0.8–1.2 mL h^{-1}, and 88 ± 1% at the flow rate of 1.4 mL h^{-1}, both of which are significantly ($p < 0.0001$) higher than the raw semen motility of 27 ± 1% (Fig. 6a). The vitality of cells increased from 42% in raw semen to 99% for the sample processed at 0.8 ml h^{-1} and remained unchanged in higher flow rates (Fig. 6b). Operating the SUN chip at flow rates of 0.8 ml h^{-1} and 1.0 ml h^{-1} resulted in a sperm population with motile cell concentration (C_{motile}) of ~8 million sperm per milliliter, while higher flow rates reduced it down to 3 million sperm per milliliter (Fig. 6c). The yield of retrieved motile sperm from raw semen is calculated by $[V \times \text{Motility\%} \times C_{motile}]_{recovered}/[V \times \text{Motility\%} \times C_{motile}]_{initial} \times 100$ where V is the volume of sample, which is 150 μL for both the loaded and collected samples. The yield maximizes at 32% when the chip is operating at a flow rate of 1 mL h^{-1}. Increasing the flow rate to 1.5 mL h^{-1} reduces the yield to 13%. Note that we did not consider the raw semen loaded to distributor channels and tubing. By considering the total loaded semen volume (180 μL), the yield of separation ranges 11–27% depending on the flow rate.

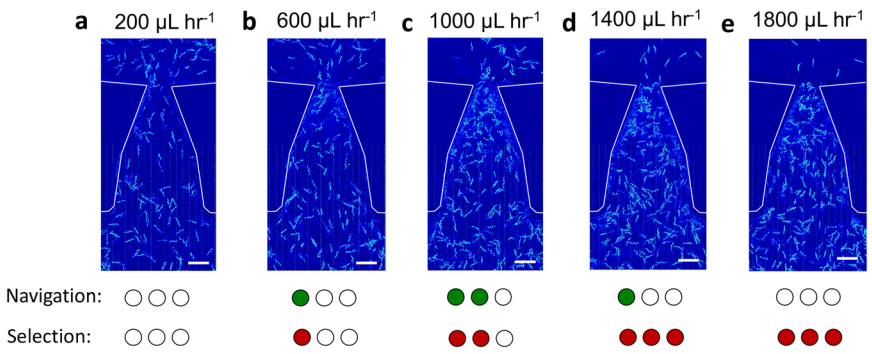

Fig. 5 Effect of the flow rate on the navigation and selection functionality of barriers. Sperm trajectories, in region 2 barriers under total inlet flow rates of 200 (a), 600 (b), 1000 (c), 1400 (d), and 1800 μL h^{-1} (e). Scale bars indicate 100 μm.

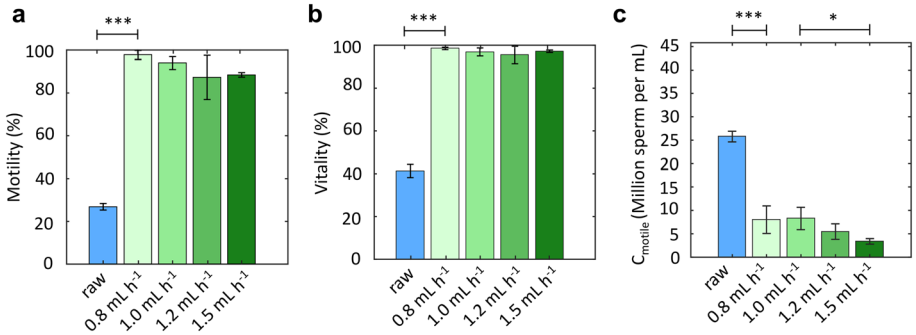

Fig. 6 Comparing the (a) motility%, (b) vitality, and (c) motile sperm concentration C_{motile} of sperm populations extracted from the SUN chip under flow rates of 0.8, 1, 1.2, and 1.5 mL h^{-1} with raw bovine semen sample (N = 3). The vitality of cells was measured by LIVE/DEAD staining. p values were determined using one-way ANOVA, *$p < 0.05$, ***$p < 0.0001$.

All velocity-related motility metrics obtained from computer assisted sperm analysis (CASA) showed significant improvement in processed samples compared to raw semen (Fig. 7a). For definitions and details of the motility metrics, see the Methods section. The overall magnitude of these metrics tended to decrease as the flow rate increased. Average path velocity (VAP) approximately doubled in isolated samples from the SUN chip, indicating a higher proportion of fast-moving sperm. Straight-line velocity (VSL) exhibited a similar trend to VAP, with an initial increase at 0.8 mL h^{-1} but a reduction at 1.5 mL h^{-1}. The amplitude of lateral head displacement (ALH) was comparable across all groups, except at the highest tested flow rate, where it increased (Fig. 7b). Across all flow rates, sperm separated by the SUN chip exhibited a higher (29 μm) beat cross frequency (BCF) than those in the raw semen sample (27 μm). However, straightness (STR) decreased at flow rates above 0.8 mL h^{-1}. Linearity (LIN) of the sperm population remained largely unchanged after processing on the SUN chip, except at the lowest flow rate (0.8 mL h^{-1}), where LIN increased.

Overall, the general improvement of velocity parameters (VSL, VCL, and VAP) indicates SUN chip's selectivity for higher motility cells. It is likely that rheotaxis based separation removed cells that have been either killed or damaged by the process of cryopreservation since velocity parameters are significantly lowered in sub-lethally damaged cells.[64] In some pairwise comparisons between flow rates, we observed a pattern emerge at the two ends of the tested range: more progressive characteristics present at low flow rates (higher values of LIN and STR, lower ALH) and less progressive (decreased LIN and STR, higher ALH) at higher flow rates. The physical explanation for the observation could be the shear rate-based sorting. Hyperactive cells have been known to move better through higher viscosity fluids[65] and, since the force per unit area generated by the flow is a function of both viscosity and shear rate, it is natural to assume that cells displaying hyperactivity-like behavior would be selected for in higher shear rate experiments.[20] The chemical and more conservative explanation might stem from the fact that seminal plasma has been known to prevent the transition of cells to a capacitated state and, since the cells were effectively washed during the processing of the semen sample, the hyperactivation characteristics might have naturally occurred due to the lack of inhibitor presence and the observed pattern across different flow rates was happenstance.[66]

The processing volume of the SUN chip is 150 μL, which is twice as large as previously reported rheotaxis-based microfluidic platforms.[7,8] Further, compared to designs with operationally-complex multiple liquid streams,[45,46] the SUN

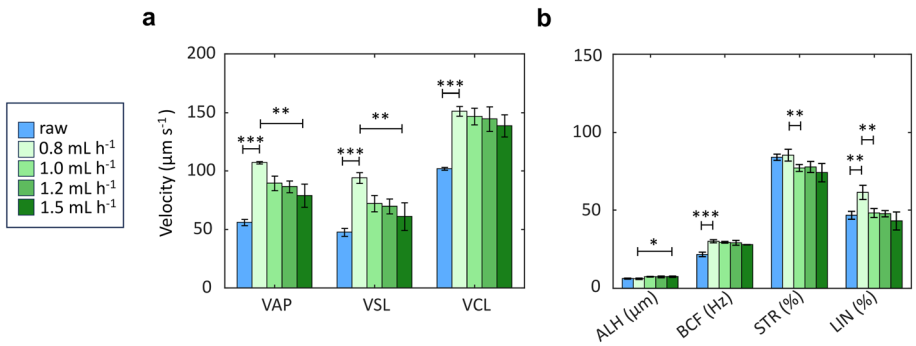

Fig. 7 Motility parameters for sperm extracted from the SUN chip at flow rates of 0.8–1.5 mL h^{-1}. (a) Straight-line velocity (VSL), curvilinear velocity (VCL), and average path velocity (VAP) were increased in processed samples. (b) Amplitude of lateral head displacement (ALH), beat cross frequency (BCF), straightness (STR), and linearity (LIN) were altered in sperm populations processed using the SUN chip. Error bars show the standard deviation within the experimental replicates. p values were determined using one-way ANOVA, *$p < 0.05$, **$p < 0.001$, ***$p < 0.0001$.

chip has one fluid stream, which makes the process more user friendly. The sample processing times between 12–22.5 min indicates a throughput of 0.75 mL h^{-1} of raw semen samples with a retrieval yield as high as ~30%. The enhanced vitality and 50% higher faster motility of sperm selected by rheotaxis has been proven to result in improved embryonic development.[8]

Several flow-based microfluidic devices that do not use rheotaxis exploited sheath laminar flow[67,68] for sperm selection. These sheath-flow based microfluidic designs operate based on diffusophoresis of motile sperm and are pumpless, which makes them user-friendly. However, they either suffer from low processing volume[67] or low motile sperm retrieval efficiency.[68] A potential limitation of pumpless sheath-flow designs is that tuning the motility level of the extracted sperm population necessitates modifying the device geometry. In contrast, rheotaxis-based systems enable precise modulation of sperm motility simply by adjusting the flow rate, while maintaining the same device configuration. Passive microfluidic devices exploit sperm boundary-following behavior.[15] Among these, parallelized channel design[69] was a successful early iteration, albeit with low processing volumes. Subsequent iterations increased throughput.[47,48] However, these devices still lack active selection pressure and precise control over the final cell population. Without such selection, the fastest sperm, which have been shown to improve embryonic development,[8] cannot be preferentially isolated.[12] Moreover, if the semen sample contains other particles, such as preservatives or, in our case, milk components, these will also diffuse into the collection zone and contaminate the final extracted sample. Rheotaxis provides a more biologically relevant mechanism, as it guides sperm toward the site of fertilization.[18,24]

Conclusion

Through a combined theoretical and experimental approach, we have demonstrated how spermatozoa navigate an outward radial flow, exhibiting distinct rheotactic behaviors depending on flow conditions. At moderate flow rates, sperm migrated toward the center, while at higher flow rates, they adopted a rotational rheotactic response, gradually spiraling inward. This work increases our understanding of the rheotactic behaviors of microswimmers in complex flow environments, potentially informing future designs of microfluidic systems for studying and manipulating other motile microorganisms, such as bacteria,[70] under dynamic flow conditions. The computational results provided the foundation for designing and optimizing the sperm unidirectional navigation (SUN) chip, which integrates controlled radial flow with strategically placed geometric strictures to enhance sperm selection efficiency. The SUN chip effectively isolates a highly motile (>93% motility) and vital sperm population, with selected cells exhibiting an average speed 50% greater than those in raw semen. By leveraging hydrodynamic selection principles, our platform surpasses conventional sperm sorting methods, offering a physiologically relevant and high-throughput approach for assisted reproductive technologies. Despite high-throughput sperm selection by our SUN chip, the final sperm concentration is limited partially due to the dependence of rheotaxis on solid boundaries[17,18] which can be overcome by parallelizing chambers and barriers of the next iteration of the SUN chip. Automation of the procedure can be achieved by converting the SUN chip to a filter-like design, similar to the sperm syringe,[47] and removing the syringe pump component by an internal flow generation mechanism. Future research can also be directed toward merging sperm preparation technologies with oocyte preparation, including oocyte denudation,[71] to achieve an automated setup for assisted reproductive techniques such as *in vitro* fertilization (IVF) and intracytoplasmic sperm injection (ICSI).

Methods

Bovine spermatozoa and medium preparation

Bovine semen samples from a healthy adult bull, preserved in 200 μL straws with a standard milk-extended preservant and stored in liquid nitrogen, were generously provided by Select Sires, Inc. (Plain City, OH, USA). Samples were thawed in a 37 °C water bath and used within two hours. A low-viscosity medium (BO-SemenPrep, IVF Bioscience) supplemented with 0.2% (w/v) bovine serum albumin (BSA) was used in experiments. The addition of BSA helped prevent sperm heads from tethering to the surfaces. The medium was pre-warmed to 37 °C before being introduced to the chip.

Device fabrication and operation

The chip was fabricated using conventional soft lithography technique.[63] The mold of the chip was designed in AutoCAD 2024, and the patterns were transferred to a silicon wafer (University Wafer) from a photomask using UV lithography. The negative photoresist SU-8 2100 (KAYAKU Advanced Materials) was coated on the wafer using spin-coating at 1700 rpm for 30 s, baked at 65 °C for 7 min and 95 °C for 35 min. Baked masks were exposed to 365 nm UV light through the pattern mask for 38 s and baked at 65 °C for 5 min and 95 °C for 13 min. The mold was subsequently developed in the SU-8 developer for 16 min. We also hard-baked the mold at 180 °C for 12 min to remove the cracks. The height of the fabricated structures was 205 ± 5 μm measured using a profilometer (KLA Tencor P7 profilometer). The mold was then cast with polydimethylsiloxane (PDMS) (Sylgard 184, Dow Corning) prepared according to the manufacturer procedure (1 : 10 elastomer base : curing agent) and cured at 65 °C for 2 h. Inlet ports were punched, and the PDMS part was plasma bonded to a glass slide. Fluid flow and temperature were controlled by a syringe pump (Chemyx) and a heated microscope stage (Carl Zeiss), respectively. To establish sperm population within the chip for navigation analysis, the chip was initially filled with raw semen samples

and then washed with the medium to remove debris and cryopreserving particles. Detailed description of device operation for sperm selection can be found in the SI (Fig. S3).

Video acquisition and image analysis

Sperm motion in the microfluidic chip was recorded using a phase-contrast microscope (Nikon Eclipse) paired with a digital camera (Phantom Ametek), capturing videos at 30 frames per second (fps) with a 10× objective lens. For the experimental investigation of sperm migration in radial flow, we used the Fiji platform[72] to manually track sperm and obtain the location of cells (x, y) over time and further processed in MATLAB (version R2024b). The instantaneous angular velocity, $\Omega(t)$, was computed as the frame-to-frame change in the cell's orientation angle with respect to x axis, $\theta(t)$, *i.e.*, $\Omega(t) = \mathrm{d}\theta/\mathrm{d}t$, where $\mathrm{d}\theta$ was calculated between consecutive frames. To reduce noise, $\theta(t)$ was smoothed with a Gaussian filter ($\sigma = 6$) prior to differentiation.

For the overlaid images of sperm migration (Fig. 4e–g and 5), the recorded frames for each barrier were analyzed using ImageJ (version 1.54g) using a multi-step image processing used previously.[21] Briefly, for each video, the minimum intensity at each pixel across all frames was calculated to map sperm presence at specific locations. The same process was repeated using the median intensity value for each pixel. By calculating the standard deviation between these two images, we generated a single image where intensity levels indicated sperm presence in specific areas over a fixed time window. The resulting gray-scale images were colorized using MATLAB (version R2024b) for enhanced visualization.

Computational methods

Fluid velocity and shear rate profiles were generated using computational fluid dynamics simulations in COMSOL Multiphysics 6.0. The simulations used the laminar flow module, modeling fluid flow through a radial geometry with a no-slip boundary condition applied to the walls and a zero static pressure condition at the outlet. The fluid is assumed to be single-phase, incompressible, Newtonian with a density of 1000 kg m^{-3} and dynamic viscosity of $\mu = 1 \times 10^{-3}$ Pa s^{-1}. Using water properties in the simulation is justified, as the actual medium has similar physical characteristics to water. Equations governing sperm movement (eqn (1) and (4)) were numerically solved by an explicit Runge–Kutta method[73] using MATLAB version R2024b. The time step size of 0.5 s is used in all simulations and equations solved for sperm until they reach either outer or inner domain boundary.

Sperm motility and vitality analysis

The vitality is determined by staining sperm with SYBR-14 fluorescent dye (Invitrogen, Thermo Fisher Scientific) according to procedure provided by the manufacturer. The live cells were counted manually, and vitality was calculated as the number of vital cells divided by total number of cells in the sample. From the CASA analysis (Hamilton Thorn, ltd.), conventional motility parameters were extracted for at least 200 sperm. The total motility(%) is the number of motile sperm divided by total sperm count; and the concentration of motile sperm is calculated by motility(%) × Total sample concentration. Average path velocity (VAP) is the speed of the cell along its mean trajectory; curvilinear velocity (VCL) is the speed of the cell moving along its actual path; straight line velocity (VSL) is the total speed of travel across the line from the first tracked location of sperm and its last tracked location. Other standard metrics were extracted from the trajectory of travel: amplitude of lateral head displacement (ALH) is the amplitude of the curvilinear path with the mean path as the central axis, and beat cross frequency (BCF) describes the frequency of the curvilinear path's intersection with the average trajectory. Then, from the preceding metrics, the remaining values were calculated: straightness (STR) is described the efficiency of travel of the spermatozoa from the starting point to the end point and is defined as VSL/VAP × 100, and linearity (LIN) shows the amount of curvilinear motion along the direction of the mean trajectory and is computed as VCL/VAP × 100.

Statistical analysis

Statistical significance of differences in motility parameters was assessed using one-way ANOVA, with $p < 0.05$ considered statistically significant. When the ANOVA indicated significant differences, *post hoc* pairwise comparisons were performed using the Tukey test. All sperm motility measurements were conducted in triplicate.

Author contributions

Ali Karimi: conceptualization, formal analysis, data curation, software, and writing – original draft. Xieergai Jiang: formal analysis, data curation, and writing – original draft. Alireza Abbaspourrad: conceptualization, funding acquisition, project administration, supervision, writing – review & editing.

Conflicts of interest

The authors declare that they have no known competing financial interests or personal relationships that could have appeared to influence the work reported in this paper.

Data availability

The data used to create the figures in this manuscript and the supporting information (SI) can be found here: https://doi.org/10.5281/zenodo.14897833.

Supplementary information: the supporting information contains additional figures, discussions and movies. See DOI: https://doi.org/10.1039/d5lc00778j.

Acknowledgements

We thank Dr. Soon Hon Cheong for providing access to the CASA system and Dr. Kelley Donaghy for assistance with proofreading and editing the manuscript. This work was conducted in part at the Cornell Nanoscale Facility, a member of the National Nanotechnology Coordinated Infrastructure (NNCI), which is supported by the National Science Foundation (Grant NNCI-2025233). The authors certify that generative AI was not used in preparing this article. Non-generative AI, such as spelling and grammar checkers in Office 365 and Google Docs, and citation managing software, was used. All instances when non-generative AI was used were reviewed by the authors and editors.

References

1 S. S. Suarez and A. A. Pacey, Sperm Transport in the Female Reproductive Tract, *Hum. Reprod. Update*, 2005, **12**(1), 23–37, DOI: 10.1093/humupd/dmi047.
2 S. S. Suarez, Mammalian Sperm Interactions with the Female Reproductive Tract, *Cell Tissue Res.*, 2016, **363**(1), 185–194, DOI: 10.1007/s00441-015-2244-2.
3 R. Nosrati, P. J. Graham, B. Zhang, J. Riordon, A. Lagunov, T. G. Hannam, C. Escobedo, K. Jarvi and D. Sinton, Microfluidics for Sperm Analysis and Selection, *Nat. Rev. Urol.*, 2017, **14**(12), 707–730, DOI: 10.1038/nrurol.2017.175.
4 M. E. Kervancioglu, E. Saridogan, R. J. Aitken and O. Djahanbakhch, Importance of Sperm-to-Epithelial Cell Contact for the Capacitation of Human Spermatozoa in Fallopian Tube Epithelial Cell Cocultures, *Fertil. Steril.*, 2000, **74**(4), 780–784, DOI: 10.1016/S0015-0282(00)01514-4.
5 N. Spassky and A. Meunier, The Development and Functions of Multiciliated Epithelia, *Nat. Rev. Mol. Cell Biol.*, 2017, **18**(7), 423–436, DOI: 10.1038/nrm.2017.21.
6 M. R. Raveshi, M. S. Abdul Halim, S. N. Agnihotri, M. K. O'Bryan, A. Neild and R. Nosrati, Curvature in the Reproductive Tract Alters Sperm–Surface Interactions, *Nat. Commun.*, 2021, **12**(1), 3446, DOI: 10.1038/s41467-021-23773-x.
7 M. Zaferani, G. D. Palermo and A. Abbaspourrad, Strictures of a Microchannel Impose Fierce Competition to Select for Highly Motile Sperm, *Sci. Adv.*, 2019, **5**(2), eaav2111, DOI: 10.1126/sciadv.aav2111.
8 M. Yaghoobi, A. Abdelhady, A. Favakeh, P. Xie, S. Cheung, A. Mokhtare, Y. L. Lee, A. V. Nguyen, G. Palermo, Z. Rosenwaks, S. H. Cheong and A. Abbaspourrad, Faster Sperm Selected by Rheotaxis Leads to Superior Early Embryonic Development in Vitro, *Lab Chip*, 2024, **24**(2), 210–223, DOI: 10.1039/D3LC00737E.
9 V. Rothschild, Non-Random Distribution of Bull Spermatozoa in a Drop of Sperm Suspension, *Nature*, 1963, **198**(4886), 1221–1222, DOI: 10.1038/1981221a0.
10 R. Nosrati, A. Driouchi, C. M. Yip and D. Sinton, Two-Dimensional Slither Swimming of Sperm within a Micrometre of a Surface, *Nat. Commun.*, 2015, **6**(1), 8703, DOI: 10.1038/ncomms9703.
11 C. Tung, F. Ardon, A. G. Fiore, S. S. Suarez and M. Wu, Cooperative Roles of Biological Flow and Surface Topography in Guiding Sperm Migration Revealed by a Microfluidic Model, *Lab Chip*, 2014, **14**(7), 1348–1356, DOI: 10.1039/C3LC51297E.
12 C. Tung, L. Hu, A. G. Fiore, F. Ardon, D. G. Hickman, R. O. Gilbert, S. S. Suarez and M. Wu, Microgrooves and Fluid Flows Provide Preferential Passageways for Sperm over Pathogen Tritrichomonas Foetus, *Proc. Natl. Acad. Sci. U. S. A.*, 2015, **112**(17), 5431–5436, DOI: 10.1073/pnas.1500541112.
13 A. Guidobaldi, Y. Jeyaram, I. Berdakin, V. V. Moshchalkov, C. A. Condat, V. I. Marconi, L. Giojalas and A. V. Silhanek, Geometrical Guidance and Trapping Transition of Human Sperm Cells, *Phys. Rev. E*, 2014, **89**(3), 032720, DOI: 10.1103/PhysRevE.89.032720.
14 R. Nosrati, P. J. Graham, Q. Liu and D. Sinton, Predominance of Sperm Motion in Corners, *Sci. Rep.*, 2016, **6**(1), 26669, DOI: 10.1038/srep26669.
15 P. Denissenko, V. Kantsler, D. J. Smith and J. Kirkman-Brown, Human Spermatozoa Migration in Microchannels Reveals Boundary-Following Navigation, *Proc. Natl. Acad. Sci. U. S. A.*, 2012, **109**(21), 8007–8010, DOI: 10.1073/pnas.1202934109.
16 V. Kantsler, J. Dunkel, M. Blayney and R. E. Goldstein, Rheotaxis Facilitates Upstream Navigation of Mammalian Sperm Cells, *eLife*, 2014, **3**, e02403, DOI: 10.7554/eLife.02403.
17 C. Tung, F. Ardon, A. Roy, D. L. Koch, S. S. Suarez and M. Wu, Emergence of Upstream Swimming via a Hydrodynamic Transition, *Phys. Rev. Lett.*, 2015, **114**(10), 108102, DOI: 10.1103/PhysRevLett.114.108102.
18 Z. Zhang, J. Liu, J. Meriano, C. Ru, S. Xie, J. Luo and Y. Sun, Human Sperm Rheotaxis: A Passive Physical Process, *Sci. Rep.*, 2016, **6**(1), 23553, DOI: 10.1038/srep23553.
19 D. J. Smith, E. A. Gaffney, H. Gadêlha, N. Kapur and J. C. Kirkman-Brown, Bend Propagation in the Flagella of Migrating Human Sperm, and Its Modulation by Viscosity, *Cell Motil. Cytoskeleton*, 2009, **66**(4), 220–236, DOI: 10.1002/cm.20345.
20 F. Yazdan Parast, A. S. Gaikwad, R. Prabhakar, M. K. O'Bryan and R. Nosrati, The Cooperative Impact of Flow and Viscosity on Sperm Flagellar Energetics in Biomimetic Environments, *Cell Rep. Phys. Sci.*, 2023, **4**(11), 101646, DOI: 10.1016/j.xcrp.2023.101646.
21 A. Karimi, M. Yaghoobi and A. Abbaspourrad, Geometry of Obstructed Pathway Regulates Upstream Navigational Pattern of Sperm Population, *Lab Chip*, 2025, **25**(4), 631–643, DOI: 10.1039/D4LC00797B.
22 S. S. Suarez, Mammalian Sperm Interactions with the Female Reproductive Tract, *Cell Tissue Res.*, 2016, **363**(1), 185–194, DOI: 10.1007/s00441-015-2244-2.
23 S. S. Suarez, K. Brockman and R. Lefebvre, Distribution of Mucus and Sperm in Bovine Oviducts after Artificial Insemination: The Physical Environment of the Oviductal Sperm Reservoir, *Biol. Reprod.*, 1997, **56**(2), 447–453, DOI: 10.1095/biolreprod56.2.447.

24 K. Miki and D. E. Clapham, Rheotaxis Guides Mammalian Sperm, *Curr. Biol.*, 2013, **23**(6), 443–452, DOI: 10.1016/j.cub.2013.02.007.
25 M. S. Abdul Halim, J. M. Dyson, M. M. Gong, M. K. O'Bryan and R. Nosrati, Fallopian Tube Rheology Regulates Epithelial Cell Differentiation and Function to Enhance Cilia Formation and Coordination, *Nat. Commun.*, 2024, **15**(1), 7411, DOI: 10.1038/s41467-024-51481-9.
26 R. H. F. Hunter, P. Coy, J. Gadea and D. Rath, Considerations of Viscosity in the Preliminaries to Mammalian Fertilisation, *J. Assist. Reprod. Genet.*, 2011, **28**(3), 191–197, DOI: 10.1007/s10815-010-9531-3.
27 M. Zaferani, F. Javi, A. Mokhtare, P. Li and A. Abbaspourrad, Rolling Controls Sperm Navigation in Response to the Dynamic Rheological Properties of the Environment, *eLife*, 2021, **10**, e68693, DOI: 10.7554/eLife.68693.
28 E. Lauga and T. R. Powers, The Hydrodynamics of Swimming Microorganisms, *Rep. Prog. Phys.*, 2009, **72**(9), 096601, DOI: 10.1088/0034-4885/72/9/096601.
29 T. Kaya and H. Koser, Direct Upstream Motility in Escherichia Coli, *Biophys. J.*, 2012, **102**(7), 1514–1523, DOI: 10.1016/j.bpj.2012.03.001.
30 A. J. T. M. Mathijssen, N. Figueroa-Morales, G. Junot, É. Clément, A. Lindner and A. Zöttl, Oscillatory Surface Rheotaxis of Swimming E. Coli Bacteria, *Nat. Commun.*, 2019, **10**(1), 3434, DOI: 10.1038/s41467-019-11360-0.
31 A. P. Berke, L. Turner, H. C. Berg and E. Lauga, Hydrodynamic Attraction of Swimming Microorganisms by Surfaces, *Phys. Rev. Lett.*, 2008, **101**(3), 038102, DOI: 10.1103/PhysRevLett.101.038102.
32 D. J. Smith, E. A. Gaffney, J. R. Blake and J. C. Kirkman-brown, Human Sperm Accumulation near Surfaces: A Simulation Study, *J. Fluid Mech.*, 2009, **621**, 289–320, DOI: 10.1017/S0022112008004953.
33 K. Ishimoto, H. Gadêlha, E. A. Gaffney, D. J. Smith and J. Kirkman-Brown, Coarse-Graining the Fluid Flow around a Human Sperm, *Phys. Rev. Lett.*, 2017, **118**(12), 124501, DOI: 10.1103/PhysRevLett.118.124501.
34 E. A. Gaffney, K. Ishimoto and B. J. Walker, Modelling Motility: The Mathematics of Spermatozoa, *Front. Cell Dev. Biol.*, 2021, **9**, 710825.
35 M. Zaferani, S. H. Cheong and A. Abbaspourrad, Rheotaxis-Based Separation of Sperm with Progressive Motility Using a Microfluidic Corral System, *Proc. Natl. Acad. Sci. U. S. A.*, 2018, **115**(33), 8272–8277, DOI: 10.1073/pnas.1800819115.
36 M. Yaghoobi, M. Azizi, A. Mokhtare and A. Abbaspourrad, Progressive Bovine Sperm Separation Using Parallelized Microchamber-Based Microfluidics, *Lab Chip*, 2021, **21**(14), 2791–2804, DOI: 10.1039/D1LC00091H.
37 A. Heydari, M. Zabetian Targhi, I. Halvaei and R. Nosrati, A Novel Microfluidic Device with Parallel Channels for Sperm Separation Using Spermatozoa Intrinsic Behaviors, *Sci. Rep.*, 2023, **13**(1), 1185, DOI: 10.1038/s41598-023-28315-7.
38 D. B. Weibel, W. R. DiLuzio and G. M. Whitesides, Microfabrication Meets Microbiology, *Nat. Rev. Microbiol.*, 2007, **5**(3), 209–218, DOI: 10.1038/nrmicro1616.
39 A. R. Jahangiri, N. Ziarati, E. Dadkhah, M. N. Bucak, P. Rahimizadeh, A. Shahverdi, M. A. Sadighi Gilani and T. R. Topraggaleh, Microfluidics: The Future of Sperm Selection in Assisted Reproduction, *Andrology*, 2024, **12**(6), 1236–1252, DOI: 10.1111/andr.13578.
40 E. T. Y. Leung, C.-L. Lee, X. Tian, K. K. W. Lam, R. H. W. Li, E. H. Y. Ng, W. S. B. Yeung and P. C. N. Chiu, Simulating Nature in Sperm Selection for Assisted Reproduction, *Nat. Rev. Urol.*, 2022, **19**(1), 16–36, DOI: 10.1038/s41585-021-00530-9.
41 M. P. B. Nagata, K. Endo, K. Ogata, K. Yamanaka, J. Egashira, N. Katafuchi, T. Yamanouchi, H. Matsuda, Y. Goto, M. Sakatani, T. Hojo, H. Nishizono, K. Yotsushima, N. Takenouchi, Y. Hashiyada and K. Yamashita, Live Births from Artificial Insemination of Microfluidic-Sorted Bovine Spermatozoa Characterized by Trajectories Correlated with Fertility, *Proc. Natl. Acad. Sci. U. S. A.*, 2018, **115**(14), E3087–E3096, DOI: 10.1073/pnas.1717974115.
42 A. Ataei, A. W. C. Lau and W. Asghar, A Microfluidic Sperm-Sorting Device Based on Rheotaxis Effect, *Microfluid. Nanofluid.*, 2021, **25**(6), 52, DOI: 10.1007/s10404-021-02453-8.
43 S. Sharma, M. A. Kabir and W. Asghar, Selection of Healthy Sperm Based on Positive Rheotaxis Using a Microfluidic Device, *Analyst*, 2022, **147**(8), 1589–1597, DOI: 10.1039/D1AN02311J.
44 C.-H. Huang, C.-H. Chen, T.-K. Huang, F. Lu, J. Y. Jen Huang and B.-R. Li, Design of a Gradient-Rheotaxis Microfluidic Chip for Sorting of High-Quality Sperm with Progressive Motility, *iScience*, 2023, **26**(8), 107356, DOI: 10.1016/j.isci.2023.107356.
45 T.-K. Huang, C.-H. Huang, P.-A. Chen, C. H. Chen, F. Lu, W.-J. Yang, J. Y. J. Huang and B.-R. Li, Development of a Thermotaxis and Rheotaxis Microfluidic Device for Motile Spermatozoa Sorting, *Biosens. Bioelectron.*, 2024, **258**, 116353, DOI: 10.1016/j.bios.2024.116353.
46 S. Zeaei, M. Zabetian Targhi, I. Halvaei and R. Nosrati, High-DNA Integrity Sperm Selection Using Rheotaxis and Boundary Following Behavior in a Microfluidic Chip, *Lab Chip*, 2023, **23**(9), 2241–2248, DOI: 10.1039/D2LC01190E.
47 F. Yazdan Parast, M. K. O'Bryan and R. Nosrati, Sperm Syringe: 3D Sorting Platform for Assisted Reproduction, *Adv. Mater. Technol.*, 2022, **7**(9), 2101291, DOI: 10.1002/admt.202101291.
48 S. A. Vasilescu, L. Ding, F. Y. Parast, R. Nosrati and M. E. Warkiani, Sperm Quality Metrics Were Improved by a Biomimetic Microfluidic Selection Platform Compared to Swim-up Methods, *Microsyst. Nanoeng.*, 2023, **9**(1), 37, DOI: 10.1038/s41378-023-00501-7.
49 E. Dadkhah, M. A. Hajari, S. Abdorahimzadeh, A. Shahverdi, F. Esfandiari, N. Ziarati, M. Taghipoor and L. Montazeri, Development of a Novel Cervix-Inspired Tortuous Microfluidic System for Efficient, High-Quality Sperm Selection, *Lab Chip*, 2023, **23**(13), 3080–3091, DOI: 10.1039/D3LC00037K.
50 N. Kashaninejad, M. J. A. Shiddiky and N.-T. Nguyen, Advances in Microfluidics-Based Assisted Reproductive

Technology: From Sperm Sorter to Reproductive System-on-a-Chip, *Adv. Biosyst.*, 2018, **2**(3), 1700197, DOI: 10.1002/adbi.201700197.

51 G. Marzano, M. S. Chiriacò, E. Primiceri, M. E. Dell'Aquila, J. Ramalho-Santos, V. Zara, A. Ferramosca and G. Maruccio, Sperm Selection in Assisted Reproduction: A Review of Established Methods and Cutting-Edge Possibilities, *Biotechnol. Adv.*, 2020, **40**, 107498, DOI: 10.1016/j.biotechadv.2019.107498.

52 J. Stevanato, R. P. Bertolla, V. Barradas, D. M. Spaine, A. P. Cedenho and V. Ortiz, Semen Processing by Density Gradient Centrifugation Does Not Improve Sperm Apoptotic Deoxyribonucleic Acid Fragmentation Rates, *Fertil. Steril.*, 2008, **90**(3), 889–890, DOI: 10.1016/j.fertnstert.2007.01.059.

53 H. Malvezzi, R. Sharma, A. Agarwal, A. M. Abuzenadah and M. Abu-Elmagd, Sperm Quality after Density Gradient Centrifugation with Three Commercially Available Media: A Controlled Trial, *Reprod. Biol. Endocrinol.*, 2014, **12**(1), 121, DOI: 10.1186/1477-7827-12-121.

54 M. Muratori, N. Tarozzi, M. Cambi, L. Boni, A. L. Iorio, C. Passaro, B. Luppino, M. Nadalini, S. Marchiani, L. Tamburrino, G. Forti, M. Maggi, E. Baldi and A. Borini, Variation of DNA Fragmentation Levels During Density Gradient Sperm Selection for Assisted Reproduction Techniques: A Possible New Male Predictive Parameter of Pregnancy?, *Medicine*, 2016, **95**(20), e3624.

55 D. Sakkas, M. Ramalingam, N. Garrido and C. L. R. Barratt, Sperm Selection in Natural Conception: What Can We Learn from Mother Nature to Improve Assisted Reproduction Outcomes?, *Hum. Reprod. Update*, 2015, **21**(6), 711–726, DOI: 10.1093/humupd/dmv042.

56 L. Robinson, I. D. Gallos, S. J. Conner, M. Rajkhowa, D. Miller, S. Lewis, J. Kirkman-Brown and A. Coomarasamy, The Effect of Sperm DNA Fragmentation on Miscarriage Rates: A Systematic Review and Meta-Analysis, *Hum. Reprod.*, 2012, **27**(10), 2908–2917, DOI: 10.1093/humrep/des261.

57 L. Simon, I. Proutski, M. Stevenson, D. Jennings, J. McManus, D. Lutton and S. E. M. Lewis, Sperm DNA Damage Has a Negative Association with Live-Birth Rates after IVF, *Reprod. BioMed. Online*, 2013, **26**(1), 68–78, DOI: 10.1016/j.rbmo.2012.09.019.

58 E. Borges Jr., B. F. Zanetti, A. S. Setti, D. P. A. F. de Braga, R. R. Provenza and A. Iaconelli Jr., Sperm DNA Fragmentation Is Correlated with Poor Embryo Development, Lower Implantation Rate, and Higher Miscarriage Rate in Reproductive Cycles of Non–Male Factor Infertility, *Fertil. Steril.*, 2019, **112**(3), 483–490, DOI: 10.1016/j.fertnstert.2019.04.029.

59 P. S. Moller, Radial Flow without Swirl between Parallel Discs, *Aeronaut. Q.*, 1963, **14**(2), 163–186.

60 A. Bukatin, I. Kukhtevich, N. Stoop, J. Dunkel and V. Kantsler, Bimodal Rheotactic Behavior Reflects Flagellar Beat Asymmetry in Human Sperm Cells, *Proc. Natl. Acad. Sci. U. S. A.*, 2015, **112**(52), 15904–15909, DOI: 10.1073/pnas.1515159112.

61 S. H. Strogatz, *Nonlinear Dynamics and Chaos: With Applications to Physics, Biology, Chemistry, and Engineering*, CRC press, 2018.

62 R. Nosrati, P. J. Graham, B. Zhang, J. Riordon, A. Lagunov, T. G. Hannam, C. Escobedo, K. Jarvi and D. Sinton, Microfluidics for Sperm Analysis and Selection, *Nat. Rev. Urol.*, 2017, **14**(12), 707–730, DOI: 10.1038/nrurol.2017.175.

63 Y. Xia and G. M. Whitesides, SOFT LITHOGRAPHY, *Annu. Rev. Mater. Res.*, 1998, **28**, 153–184, DOI: 10.1146/annurev.matsci.28.1.153.

64 H. A. Mofadel, H. A. Hussein, H. H. Abd-Elhafee and T. M. El-Sherry, Impact of Various Cryo-Preservation Steps on Sperm Rheotaxis and Sperm Kinematics in Bull, *Sci. Rep.*, 2024, **14**(1), 11403, DOI: 10.1038/s41598-024-61617-y.

65 S. s. Suarez and X. Dai, Hyperactivation Enhances Mouse Sperm Capacity for Penetrating Viscoelastic Media1, *Biol. Reprod.*, 1992, **46**(4), 686–691, DOI: 10.1095/biolreprod46.4.686.

66 S. T. Mortimer, M. A. Swan and D. Mortimer, Effect of Seminal Plasma on Capacitation and Hyperactivation in Human Spermatozoa, *Hum. Reprod.*, 1998, **13**(8), 2139–2146, DOI: 10.1093/humrep/13.8.2139.

67 B. S. Cho, T. G. Schuster, X. Zhu, D. Chang, G. D. Smith and S. Takayama, Passively Driven Integrated Microfluidic System for Separation of Motile Sperm, *Anal. Chem.*, 2003, **75**(7), 1671–1675, DOI: 10.1021/ac020579e.

68 K. Matsuura, M. Takenami, Y. Kuroda, T. Hyakutake, S. Yanase and K. Naruse, Screening of Sperm Velocity by Fluid Mechanical Characteristics of a Cyclo-Olefin Polymer Microfluidic Sperm-Sorting Device, *Reprod. BioMed. Online*, 2012, **24**(1), 109–115, DOI: 10.1016/j.rbmo.2011.09.005.

69 L. Eamer, M. Vollmer, R. Nosrati, M. C. San Gabriel, K. Zeidan, A. Zini and D. Sinton, Turning the Corner in Fertility: High DNA Integrity of Boundary-Following Sperm, *Lab Chip*, 2016, **16**(13), 2418–2422, DOI: 10.1039/C6LC00490C.

70 J. Elgeti, R. G. Winkler and G. Gompper, Physics of Microswimmers—Single Particle Motion and Collective Behavior: A Review, *Rep. Prog. Phys.*, 2015, **78**(5), 056601, DOI: 10.1088/0034-4885/78/5/056601.

71 A. Favakeh, A. Mokhtare, H. Zhang, Y. A. Ren and A. Abbaspourrad, On-Chip Oocyte Cumulus Removal Using Vibration-Induced Flow, *Lab Chip*, 2025, **25**(21), 5551–5562, DOI: 10.1039/D5LC00414D.

72 J. Schindelin, I. Arganda-Carreras, E. Frise, V. Kaynig, M. Longair, T. Pietzsch, S. Preibisch, C. Rueden, S. Saalfeld, B. Schmid, J.-Y. Tinevez, D. J. White, V. Hartenstein, K. Eliceiri, P. Tomancak and A. Cardona, Fiji: An Open-Source Platform for Biological-Image Analysis, *Nat. Methods*, 2012, **9**(7), 676–682, DOI: 10.1038/nmeth.2019.

73 J. R. Dormand and P. J. Prince, A Family of Embedded Runge-Kutta Formulae, *J. Comput. Appl. Math.*, 1980, **6**(1), 19–26, DOI: 10.1016/0771-050X(80)90013-3.

